

Correlative Microstructural Analysis of a Weathered Nantan Meteorite Fragment

Graeme J. Francolini^{a,*}, Brendan V. Dyck^b, Paul Mack^c and Ben Britton^a

^aDepartment of Materials Engineering, University of British Columbia, Vancouver, V6T 1Z4, British Columbia, Canada

^bDepartment of Earth and Environmental Sciences, University of British Columbia, Kelowna, V1V 1V7, British Columbia, Canada

^cThermoFisher Scientific

arXiv:2604.14187v1 [physics.geo-ph] 31 Mar 2026

ARTICLE INFO

Keywords:

Correlative Electron Microscopy

Microanalysis

Meteorites

EDS

XPS

ABSTRACT

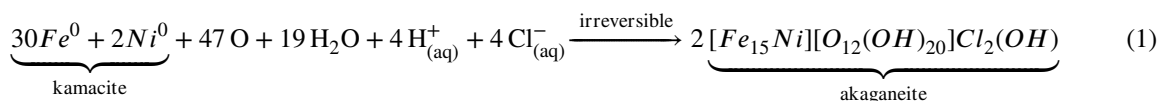
The weathering of iron-rich phases within meteorites is a multi-stage process that significantly alters the microstructure and chemical composition based both on the environmental condition at the location of landing and the exposure time since the fall. This work investigates the resulting phases of this process in a correlative and comparative manner using a naturally weathered Nantan meteorite fragment. Techniques including X-ray Photoelectron Spectroscopy, Energy Dispersive X-ray Spectroscopy, and X-ray Fluorescence Spectroscopy were used for compositional determination and X-ray Diffraction and Electron Backscatter Diffraction for phase determination and microstructural analysis.

Use of these techniques revealed the meteorite matrix to be predominantly composed of magnetite, with distinct regions of high Ni content. The grain structure was found to be very fine (approx. 5 μm) in areas of high Ni (≥2.6 at%) content with a visible boundary of 100-200 μm extending into the low Ni (≤0.9 at%) regions, wherein the grains averaged 10s of μm in size. Other common products of weathering, including goethite, lepidocrocite, and ferrosityte, were also found within the matrix alongside Ni(OH)₂. Additionally, a brecciated phase was found within the sample and appeared to be a large cohenite grain which exhibits signs of aqueous weathering, including in a vein-like structure, composed of NiO and magnetite, and deposits of iron and nickel carbonates. These results indicate that the distinct matrix regions formed through the weathering mechanism of discrete primary phases, with the high Ni regions forming from aqueous alteration of kamacite and the low Ni regions forming from direct dissolution and oxidation of the source Fe-Ni metal.

1. Introduction

To understand the fall-to-find timeline of meteorites and how best to store and preserve these rare extra-terrestrial materials it is important to understand the weathering of meteorites, including how it occurs and how it changes the material. This is especially relevant for iron meteorites including the IAB complex iron meteorites, which consist primarily of iron-nickel alloys species (kamacite, taenite, tetrataenite) and mineral inclusions. However, these meteorite phases undergo chemical modification through weathering, both terrestrially and in space. Often weathering results in a notable change in the metallic and mineral phases present, as well as changes in trace elemental compositions of meteorites.

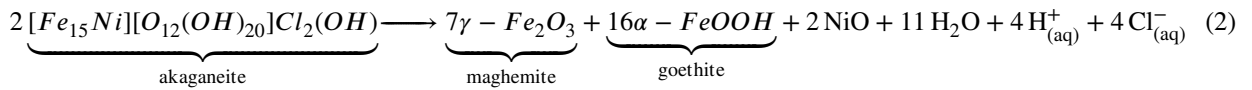
According to the literature, the terrestrial weathering process of iron-based phases is proposed to occur through two possible mechanisms. The first mechanism is a multi-step process, with Fe-Ni phases transitioning to the chlorine stabilized oxyhydroxide akaganeite, followed by decomposition into other iron oxide and oxyhydroxide species (Eq. 1 and 2) Binzel, Walker and Cameron (2006).



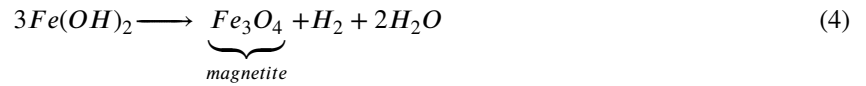
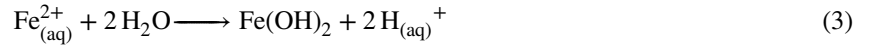
*Corresponding author

✉ graeme.francolini@ubc.ca (G.J. Francolini); ben.britton@ubc.ca (B. Britton)

ORCID(s): 0009-0007-2061-7744 (G.J. Francolini); 0000-0002-6581-5695 (B.V. Dyck); 0000-0001-5343-9365 (B. Britton)



The second mechanism is the conversion of the Fe-Ni metal into magnetite through dissolution and subsequent hydrolysis (Eq. 3) and oxidation (Eq. 4) of dissolved Fe^{2+} and Fe^{3+} ions, respectively Bland, Sexton, Jull, Bevan, Berry, Thornley, Astin, Britt and Pillinger (1998); Buchwald and Clarke (1989); Faust, Fahey, Mason and Dwornik (1973).



Furthermore, the extent of weathering experienced by meteorites is affected by the climate of the fall site. Previous work by Bland *et al.* Bland *et al.* (1998) has shown a relation between the presence of magnetically ordered species (magnetite and maghemite) and paramagnetic species (akaganeite, goethite, lepidocrocite) with the climate which chondrite meteorites landed. A high abundance of magnetically ordered species were found in meteorites which landed in humid regions; whereas magnetite is uncommon for Antarctic samples Bland *et al.* (1998). Additionally, “hot” desert meteorites have been found to contain higher contents of sulfates, Ca-carbonate, and silica as compared to Antarctic finds Binzel *et al.* (2006); Lee and Bland (2004). The difference in weathering climate also results in differences within the post-weathering microstructure. Both hot and cold climates result in predominantly Fe,Ni metal-based modification which forms vein-like structures in the metal surface. However, weathering of “hot” desert meteorites causes greater amounts of brecciation and dissolution compared to cold desert weathering Lee and Bland (2004).

This brecciation and vein-like microstructure has been observed previously through the use of scanning electron microscopy (SEM) in both chondrite and iron meteorites van Ginneken, Debaille, Decrée, Goderis, Woodland, Wozniakiewicz, De Ceukelaire, Leduc and Claeys (2022); Gurdziel (2015). These vein-like structures are typically observed intersecting or surrounding Fe,Ni metal surfaces and are composed of iron oxides and oxyhydroxides, due to dissolution of high-Fe content phases and subsequent precipitation of dissolved Fe. Individual iron oxyhydroxide species have also been observed under SEM as distinct phases that formed during low-temperature recrystallization. Goethite may appear as a globular van Ginneken *et al.* (2022) or large and angular platelet Karwowski and Gurdziel (2009) structure. Akaganeite is found to have a “cigar-shaped” or “cotton-ball” structure van Ginneken *et al.* (2022). Lastly, lepidocrocite is forms as thin and fine plates van Ginneken *et al.* (2022); Karwowski and Gurdziel (2009).

Prior work has identified these weathering phases have been identified using energy dispersive X-ray spectroscopy (EDS), Mössbauer spectroscopy van Ginneken *et al.* (2022); Bender Koch and Buchwald (1994) and electron probe microanalysis (EPMA) Lee and Bland (2004). However, in these works the elemental composition of Fe, Ni, and O can vary significantly between individual samples and weathered metallic regions in a sample. In the work of Van Ginneken *et al.* samples that underwent artificial weathering had variation of 22.9 - 44.4 wt%O, 49.2 - 67.5 wt%Fe, and 1.6 - 15.0 wt%Ni van Ginneken *et al.* (2022). For oxides, this variation has been seen to be 58.4 - 84.1 wt% Fe_2O_3 and 0.6 - 15.3 wt%NiO Lee and Bland (2004).

Significant work has also been performed to measure the composition of meteorites and to determine how their composition is altered through weathering. A variety of X-ray based methods are used to determine the elemental composition, such as EDS, X-ray Photoelectron Spectroscopy (XPS), and X-ray Fluorescence spectroscopy (XRF). These techniques are rarely used alone, instead they are often paired with other techniques to provide a better understanding of a specific material property. For example, XPS is commonly paired with other techniques to evaluate chemical states of individual elements, such as EPMA and atomic force microscopy (AFM) Pirim, Pasek, Sokolov, Sidorov, Gann and Orlando (2014). Leedahl *et al.* Leedahl, Korolev, Zhidkov, Skornyakov, Anisimov, Belozarov, Kukhareno, Kurmaev, Grokhovskii, Cholakh and Moewes (2016) investigated how the composition and oxidative state of Fe and Ni-bearing phases affects the Curie temperature using XPS. Chaves *et al.* evaluated the effects of simulated space weathering Chaves, Thompson, Loeffler, Dukes, Szabo and Horgan (2023). EDS is typically used as a complementary technique alongside SEM and X-ray Diffraction (XRD) to identify phases or evaluate the composition of elementally similar but polymorphically distinct phases Goryunov, Varga, Dankházi, Felner, Chukin, Kuzmann, Homonnay, Grokhovsky and Oshtrakh (2023). EDS has also been used with XRF and X-ray microtomography to provide a three dimensional structural, compositional, and phase understanding of meteorites Machado, de Araújo, Leitão, dos Anjos, de Oliveira and Lopes (2025). Additionally, XRF has the unique benefit that can be used as

a handheld characterization tool, allowing for bulk analysis with minimal or no sample preparation Allegretta, Marangoni, Manzari, Porfido, Terzano, De Pascale and Senesi (2020); Gemelli, D'Orazio and Folco (2015), and potentially deployed in the field.

This present study aims to investigate the chemical and microstructural modification resulting from weathering of the Nantan meteorite through a multi-modal microstructural and chemical analysis using Electron Backscatter Diffraction (EBSD), EDS, XRD, XPS, and XRF. These techniques have been applied to explore changes in the elemental composition and phases of a material, resulting from weathering, which are expected to cause significant modifications to the matrix microstructure and grain structure and warrants further investigation.

2. Materials and Methods

2.1. Material Preparation

A Nantan meteorite sample (sourced from Rocks & Gems Canada, Whistler, BC) was secured to a standard SEM stub using silver paint and super glue, then metallographically polished using an Allied High Tech Multiprep Precision Polisher, with active sample rotation and oscillation. The sample was prepared using 600, 800, and 1200 grit SiC, followed by 6 and 1 μm monocrystalline diamond suspensions and finally a 0.05 μm colloidal alumina/silica suspension. Each polishing step was performed at 250 RPM for 15 minutes, with 3 minute on pad water cleaning steps performed between the 6 μm - 0.05 μm steps. Finally, the sample was rinsed with ethanol and dried using hot air.

2.2. Material Analysis

A variety of analysis techniques and systems were used to perform microstructural and chemical analysis of the Nantan sample. For simplicity, this section has been separated into the individual systems used for the analysis.

2.2.1. Electron-based Chemical Mapping and Imaging

Secondary electron (SE), Backscatter electron (BSE) microscopy, and EDS mapping were performed on an Apreo 2 ChemiSEM (ThermoFisher). Data was collected at 20 kV with a probe current of 4 nA. The MAPS software allows for an integrated workflow and large area “montage”-based image stitching. Stitching was performed in MAPS with a 10 % tile overlap. The following maps were collected:

1. Large area (Fig. 1 a) - 27x60 tile montage, 0.293 μm pixel size and 26.51 μs dwell time. EDS mapping, BSE, and SE, data was collected.
2. Higher resolution (Fig. 1 b) - 18x20 tile montage, 0.1 μm pixel size and 88.4 μs dwell time.

The EDS data was collected with a Truesight Pro 70 detector and quantified in MAPS. SE was collected with the Everhart–Thornley (ET) detector. BSE was collected with the in-column trinity T1 detector.

2.2.2. Local Phase Identification + Crystallographic Mapping

Electron microscopy was performed on a Tescan AMBER-X plasma focused ion beam-scanning electron microscope (pFIB-SEM). All data was captured using a 10 nA beam current and 20 kV accelerating voltage. EBSD was performed using an Oxford Instruments Symmetry S2 detector and the sample loaded into a 70° pre-tilted sample holder. EDS data was captured using an Oxford Instruments Ultim Max 170 detector and the Pulse Pile up correction was enabled.

EBSD was captured both independently and in tandem with EDS using Oxford Instruments PhaseID method. The independent EBSD data was captured at a working distance of 13.8 mm, an acquisition speed of 1393.7 Hz, a resolution of 156x128 pixels, a step size of 0.5 μm , and an exposure time of 0.7 ms.

Three regions of interest were analyzed using a combination of EDS and EBSD to identify the possible material phases present in the meteorite surface. The specific parameters for each region are given in table 1. Post-acquisition analysis of the data was performed in Aztec. Additional analysis of the EBSD data was performed in Aztec Crystal using MapSweeper which performed a ‘template matching’ approach to compare the captured diffraction patterns to a dynamical-diffraction based simulation of each identified phase, thus improving the indexing precision Winkelmann, Jablon, Tong, Trager-Cowan and Mingard (2020). Followed by cross correlation coefficient filtering on an individual phase basis using the MTEX 5.10.2 package Bachmann, Hielscher and Schaeben (2010).

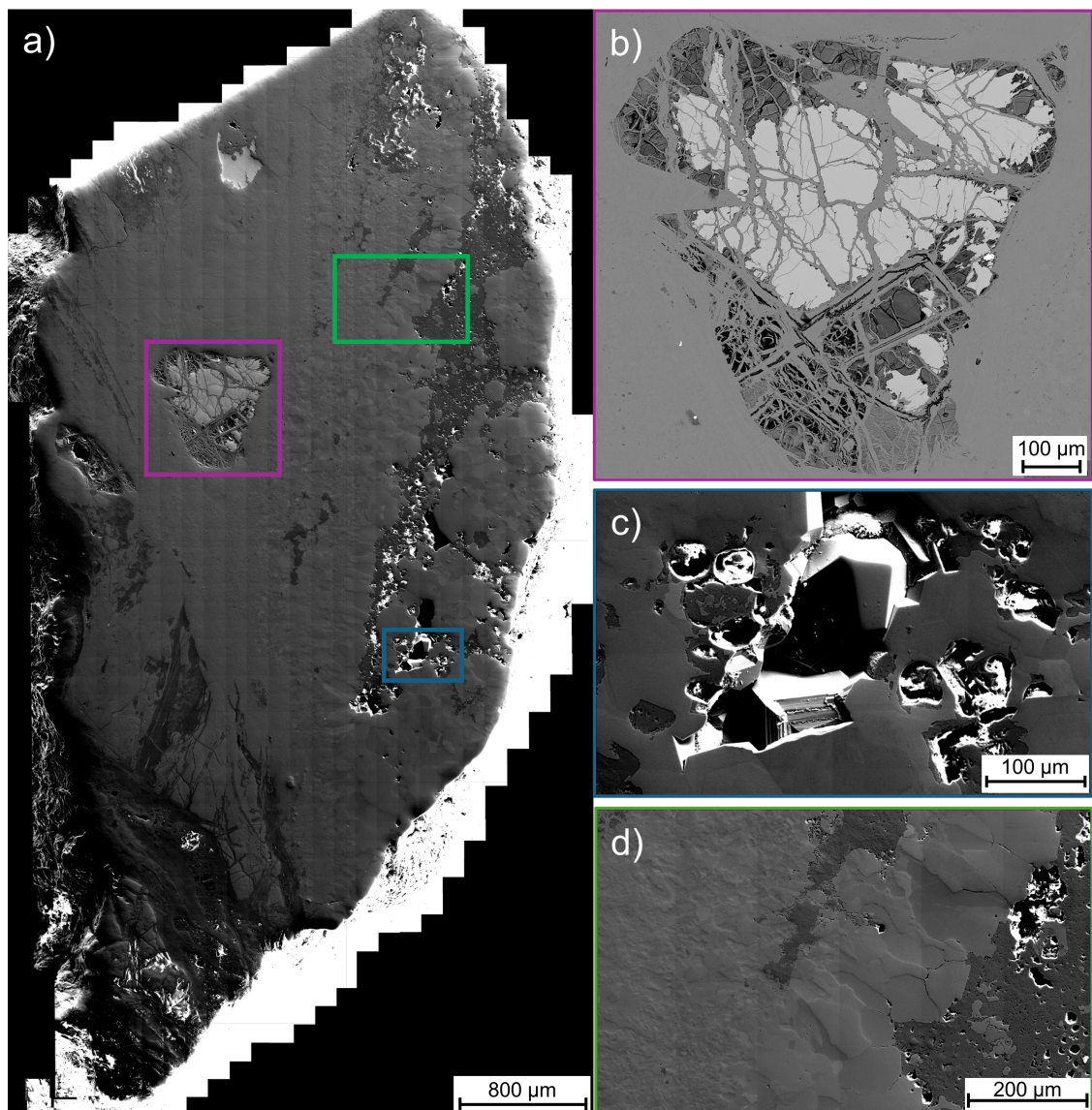


Figure 1: a) Large area secondary electron map of polished Nantan meteorite sample. b) Backscatter electron image of large inclusion present on meteorite surface (purple box). c) Large faceted crystals present within cracks on the sample surface (blue box). d) Grain structure transition region from small grains to large elongated grains. C) and d) are subset images taken from the larger stitched map (a).

2.2.3. X-ray Diffraction - Bruker D6 PHASER

XRD was performed using a Bruker D6 Phaser Tabletop XRD with a LYNXEYE XE-T detector and a Cu $\kappa - \alpha$ anode. The polished face of the Nantan sample was analyzed in a coupled two theta/theta scan at an anode voltage of 40 kV and current of 15 mA, with a continuous PSD fast scan mode. Data was collected over a 2θ range of 10° to 140° .

2.2.4. X-ray Photoelectron Spectroscopy - Thermo Scientific Nexsa G2

XPS spectra were acquired using a Thermo Scientific Nexsa G2 system with a Al K-Alpha X-ray source. The sample was cleaned using Ar^+ sputtering at 1 keV. Two areas of the sample were analyzed, the inclusion region of interest shown in 1 b) and the sample matrix. Each of these areas were analyzed using a general XPS survey followed by higher resolution single element (Fe, O, Ni) scans.

Region of Interest	1	2	3
Working Distance (mm)	6.8	13.4	6.4
Acquisition Speed (Hz)	833.28	576.30	1136.89
Resolution (pixels)	622x512	1244x1024	156x128
Step Size (μm)	5	1	0.5
Exposure Time (ms)	3.0	1.5	7.1

Table 1
EBSD data capture parameters for phase identification.

The survey of the matrix was performed in a fixed analyzer transmission mode and a constant analyzer energy (CAE) of 200. A total of five scans were performed with a 1 eV pass energy and microfocus X-ray spot size of 200 μm . The individual element scans were performed with a CAE of 50, 0.1 eV pass energy and a step and spot size of 200 μm over 10, 10, and 8 scans for Fe2p, O1s, and Ni2p respectively. All parameters for analysis of the inclusion region (overall and individual elements) were kept the same as for the matrix, except the number of scans for Fe2p which was increased to 9 scans.

2.2.5. X-ray Fluorescence Spectroscopy - IXRF Atlas μ -XRF

XRF analysis was performed using an IXRF Atlas μ -XRF system with a Rh anode and four Amptek silicon drift detectors (each with 70 mm² active areas). A large area scan of the entire polished sample surface was performed with a current of 800 nA, 50 kV voltage, 20 μm step size, 20 μm spot size and a 10 ms dwell time. Spectral data was then extracted from the overall scan data for three regions of interest (11x11 pixels) where the Fe, Mn and Ni content were observed to vary significantly.

3. Results

Preliminary investigation of the Nantan fragment using SEM showed a large variety of phases and structural morphology of the sample surface. As seen in Fig. 1, the different phases of the material appear to be sequestered in discrete areas of the sample. The upper left region of Fig. 1 a) shows a finer grained matrix with faint vein-like structure and large BSE-bright phases present (Fig. 1 b). While the matrix on the right side of the sample was made up of larger grains of varied sizes as well as voids in the surface that are infilled with an assemblage of crystalline phases (Fig. 1 c). The matrix grain structure was also observed to vary along the horizontal centre of the sample, with a distinct transition from smaller equiaxed grains on the left to large elongated grains on the right in Fig. 1 d).

Investigation of the chemical composition and distribution in the Nantan fragment using EDS identified the surface to be composed of Fe, Ni, Ca, Si, and O (Fig. 2 a). The sample consisted primarily of iron oxides, of varying stoichiometry and regions of higher Ni content. Si was observed near the multiphase crystalline region shown in Fig. 1 c) and concentrated in the BSE-darker region on the lower left of the sample. Ca was primarily observed as vein-fill within the brecciated grain in Fig. 1 b). Additional analysis using XPS (Fig. 2 b) and XRF (Fig. 2 c) corroborated the presence of regions with high Ni concentration.

The XPS maps (Fig. 2 b) showed the same spatial distribution of the Ni and Fe content as was found using EDS. However, XPS additionally allowed for the identification of different Ni species and iron oxide stoichiometry between the cracked precipitate inclusion (Fig. 1 b) and the matrix. From the XPS spectra (Fig. 3), peaks corresponding to NiO, FeO, and metallic iron were identified within the inclusion. The species identified in the matrix were primarily in the form of Fe₃O₄ and Ni as Ni(OH)₂.

The next step of characterizing the sample was to determine what mineral phases were present. This was done in two stages: (1) using XRD to obtain a range of possible mineral phases; and (2) using a combination of EDS and EBSD through Oxford Instrument's PhaseID method. The experimentally obtained XRD spectrum is given in Fig. 4 alongside XRD spectra simulated using VESTA Momma and Izumi (2011). The minerals compared to the experimental spectra were chosen due to their elemental similarity and their common presence within iron meteorites (kamacite, taenite, tetrataenite) and common products of weathered iron phases in both iron and chondrite meteorites.

Comparison of the Nantan XRD spectrum showed a strong correlation to magnetite and a weak correlation to goethite (α -FeO(OH)). No other correlations were identified from the experimental spectrum for other iron oxides, such as hematite, though it is noted the XRD analysis was performed on a singular polished face of the Nantan fragment

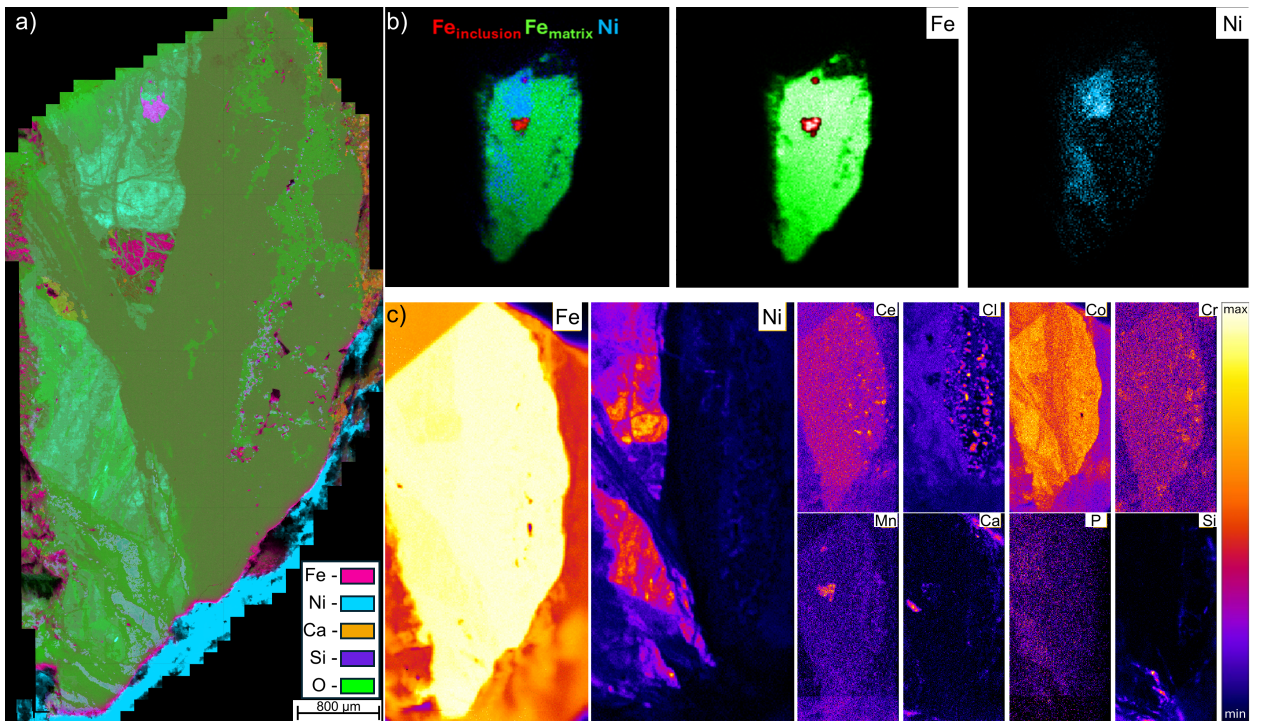


Figure 2: a) Large area EDS map of Nantan meteorite sample showing the distribution of detected elements. b) XPS SnapMaps of Nantan fragment showing the distribution of Fe and Ni. c) XRF maps of individual elements detected, with a focus on Fe and Ni.

and therefore risks preferential composition at the flat face. The Nantan fragment was also confirmed to be magnetic, further corroborating that the sample composition is a majority magnetite.

Simultaneous EBSD and EDS was performed at three regions on the sample surface with distinct and different phases. The region in Fig. 5 a) contained large elongated grains, a region of BSE-darker phase, and voids with crystalline phases inside. The matrix in this region was comprised of magnetite and no distinct phase identification was possible for the crystalline phases or darker region. The inverse pole figures (IPF) from EBSD also showed no local microtexture in the microstructure. However, there is a significant change in size and morphology of the magnetite grains as one crosses the BSE-darker region. Comparison of the experimentally obtained electron backscatter pattern (EBSP) and a dynamically simulated EBSP for magnetite also showed significant confidence in the magnetite identification for the matrix. EBSD of the second region (Fig. 5 b) showed a similar result to the first, with the matrix being identified as magnetite and low confidence for identification of other phases. However, a significant difference in the matrix grain structure was seen in this region. The magnetite grains in this region were seen to vary in size with smaller grains being closer to the high Ni content region shown in Fig. 2. Analysis of the final region showed both magnetite and goethite present on the sample surface. Though the grain structuring of goethite was not well resolved due to the concave topography in the region.

The final region analyzed using EBSD and EDS was the inclusion region shown in Fig. 1 a). EDS analysis of this region showed relative enrichment of C and Fe in the brecciated phase which appears lighter under BSE (Fig. 6). The vein-like structure and BSE-darker phase surrounding the brecciated phase were found to contain Fe, Ni, and O. Ca was also found to be present in small pockets in the inclusion, similar to the previously shown large area EDS mapping. Based on these results, the BSE-lighter phase may be composed of an iron carbide while the veins-like structure are extensions of the sample matrix and are composed of an iron oxide and nickel oxide mixture.

EBSD analysis of this region showed a unique grain structure where the phase with the highest backscatter coefficient (white in the BSE image) for the inclusion was a single grain of near-uniform orientation. This grain is brecciated, with an ‘infill’ of fine grain vein-like structures extending outward from the matrix (Fig. 7). The surrounding matrix is made up of large randomly oriented grains that decrease in size nearest the inclusion. The vein-like structure

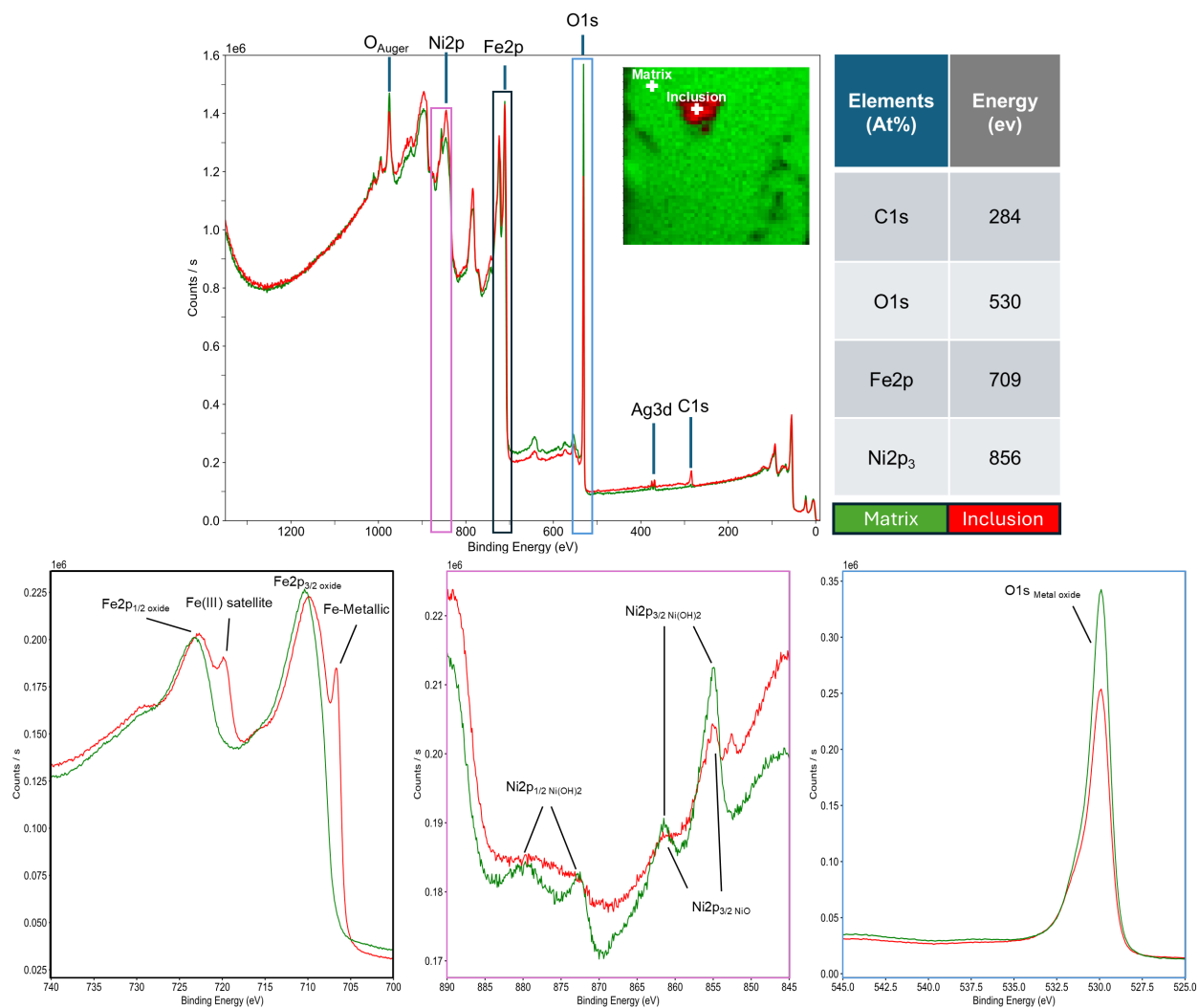


Figure 3: Overlaid XPS spectra taken at the large inclusion (red) and matrix (green) next to the elemental composition at both point, with the respective peak energies (top). Overlaid XPS spectra for XPS surveys of Fe, Ni, and O.

can also be seen within the grain structure of the matrix with the grains of the vein-like structure being relatively uniformly structured along the path of the vein while the surrounding grains of the matrix are equiaxed but random. Additionally, the phase colour map showed agreement that the matrix was composed of magnetite while the white phase were composed of cohenite/iron carbide. The other phases within the inclusion were not able to be identified using EBSD.

The elemental composition of the matrix and inclusion were investigated using XPS, EDS, and XRF, with high Ni and low Ni regions of the matrix analyzed separately for XRF and EDS (Fig. 8). The elemental composition and the identified phases for each region are given in Table 2.

Investigation of elemental composition with XRF again corroborated the distinct regions of Ni and Fe content as seen in XPS and EDS. However, XRF identified the possible presence of significantly more elements than EDS or XPS (Fig. 2 c). It is not believed that each of these elements are present within the Nantan fragment in any significant concentration, as direct analysis of the XRF spectra at the three regions of interest shown in Fig. 8 did not indicate substantial peaks from elements other than Fe and Ni. Rather, the additional elements identified by XRF are likely present only at trace levels, reflecting the sensitivity of XRF to minor and trace constituents compared to XPS. They

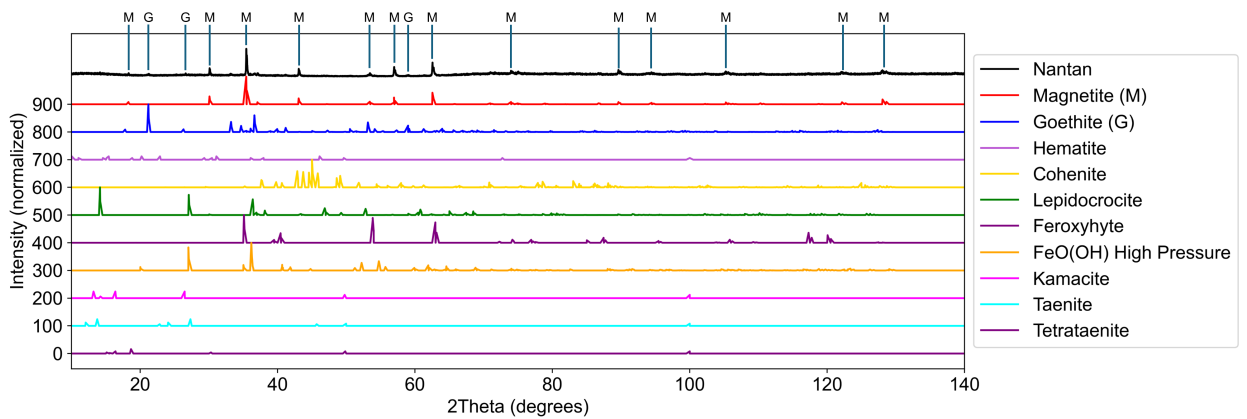


Figure 4: Experimentally obtained XRD spectrum stacked on simulated XRD spectra from common minerals in iron meteorites. The CIF files for each simulated pattern are provided in the supplementary data.

XPS (at%)	Matrix (High Ni)	Matrix (Low Ni)	Inclusion
Fe	29.29±0.29	N/A	32.43±0.59
Ni	2.67±0.13	N/A	0.61±0.16
O	66.31±0.30	N/A	54.99±0.52
C	1.43±0.13	N/A	11.70±0.26
Cl	0	N/A	0
Si	0	N/A	0
Co	0	N/A	0
EDS (at%)	Matrix (High Ni)	Matrix (Low Ni)	Inclusion
Fe	27.8±0.1	31.7±0.1	37.7±0.1
Ni	2.8±0.1	0.2±0.1	0.8±0.1
O	55.6±0.3	54.8±0.3	33.4±0.1
C	13.4±0.1	13.1±0.1	27.8±0.1
Cl	0	0	0
Si	0.3±0.1	0.2±0.1	0.2±0.1
Co	0	0	0
XRF (at%)	Matrix (High Ni)	Matrix (Low Ni)	Inclusion
Fe	87.73±0.22	98.29±0.24	96.93±0.24
Ni	10.08±0.12	0.17±0.02	1.78±0.05
O	0	0	0
C	0	0	0
Cl	0.07±0.06	0.02±0.05	0.34±0.06
Si	0.27±0.14	0.21±0.13	0.12±0.13
Co	0.94±0.05	0.42±0.05	0.51±0.05
Phases	Magnetite (I), Ni(OH) ₂ , Goethite (O), Hematite (T)	Magnetite (I)	Magnetite (I), Fe ₃ C (O), Cohenite (O), NiO (R)

Table 2

Elemental composition of the Nantan sample found using XPS, EDS, and XRF at the three regions of interest identified using XRF in Fig. 8. XPS was only captured at the high Ni section of the matrix and the inclusion. Crystal structures: (I) = Inverse spinel, (O) = Orthorhombic, (T) = Trigonal, (R) = Rock salt.

are therefore included to illustrate the differences in elemental detection capabilities among the techniques rather than to suggest meaningful compositional contributions.

The elemental composition for the high Ni matrix region and the inclusion to be very similar for EDS and XPS. The Ni and Fe concentrations were found to be notably higher using XRF. This is anticipated as XRF was unable to identify the presence of O or C. Additionally, XRF has a significantly greater interaction (excitation) depth than

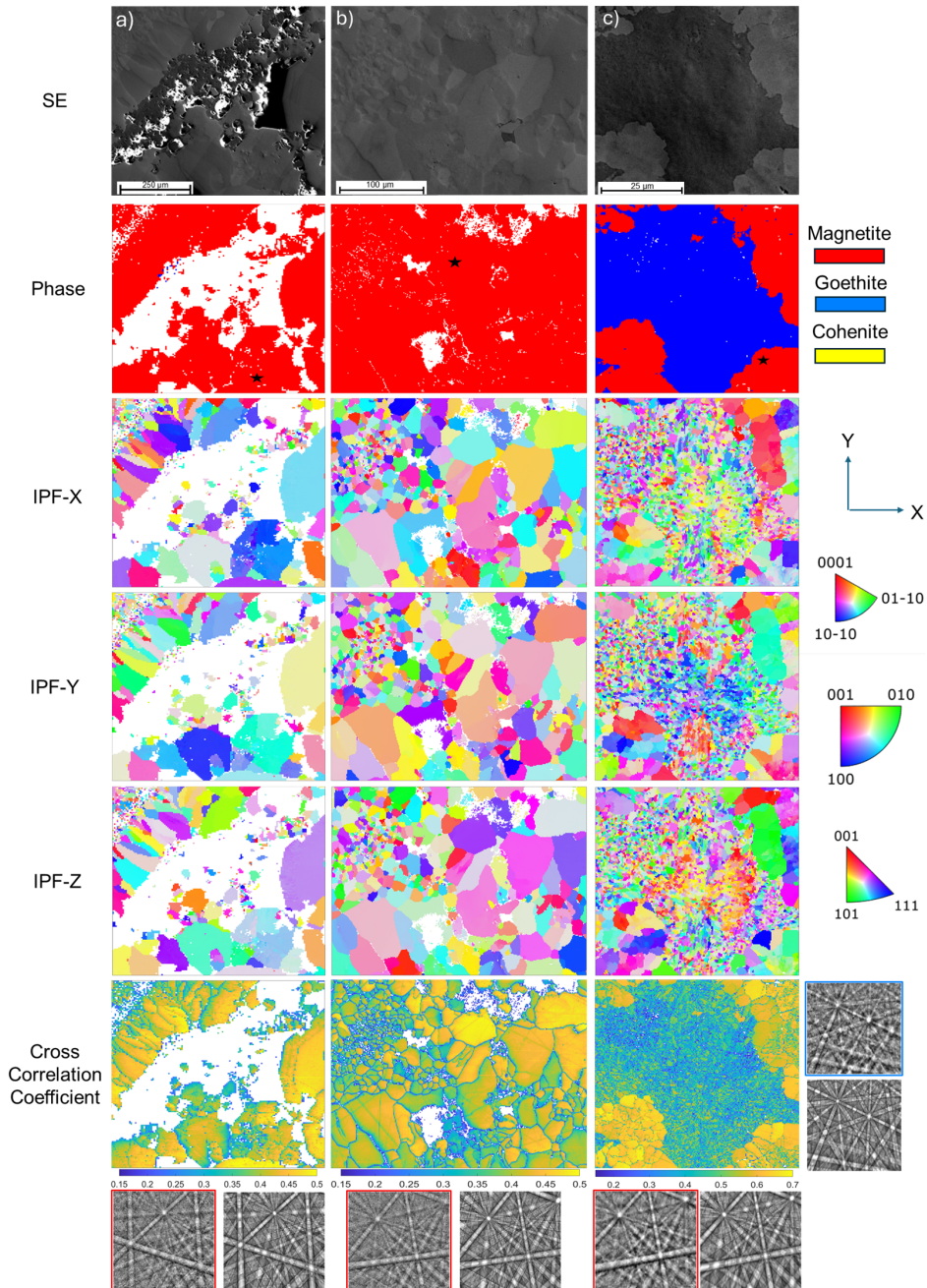


Figure 5: SE and EBSD data captured for phase identification at three regions of interest. EBSD data includes phase colour map, Inverse Pole Figure (IPF) for x, y, and z direction, cross correlation coefficient, and the electron backscatter pattern for magnetite (red boxes) and goethite (blue box).

electron-beam EDS, probing deeper into the bulk material rather than being limited to near-surface regions, which can further contribute to differences in the measured elemental concentrations. These elements have been confirmed to be present using the other analysis methods and therefore the lack of these elements in the quantification of the XRF skews the Ni and Fe composition to be higher than in reality. For example, the Fe concentration of the high Ni region is 91.7, 90.0, and 87.73 (at%) when O and C are omitted, for XPS, EDS, and XRF respectively.

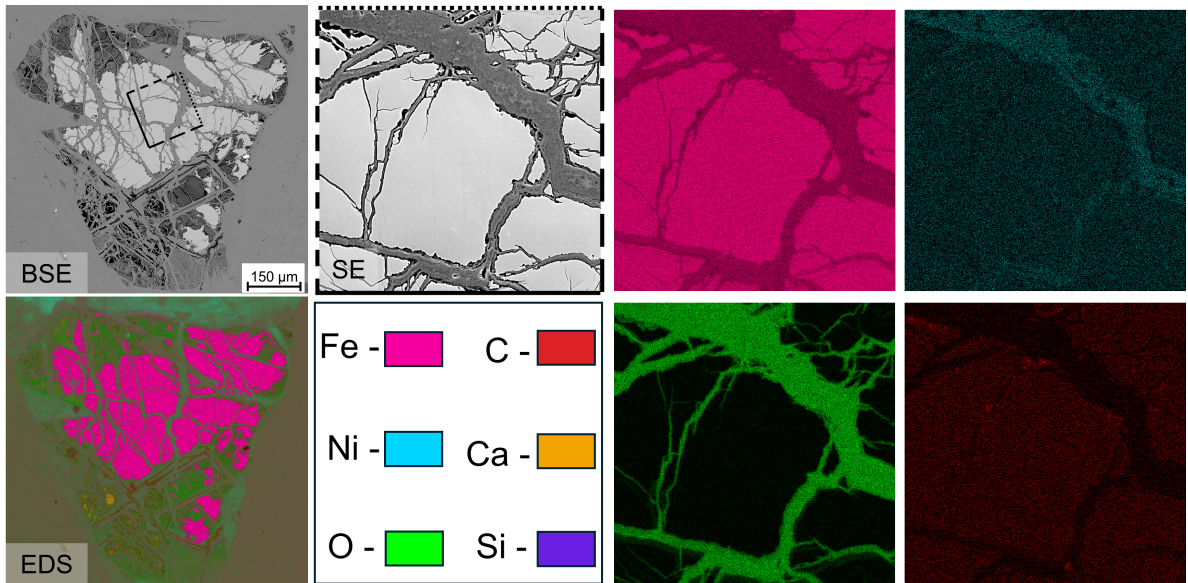


Figure 6: BSE, EDS, and SE images of large inclusion in the Nantan fragment. Overview of the inclusion is given on the left with a stitched EDS map. An increased magnification SE and EDS images are provided to the right of the area shown with the black box.

The Fe composition of the matrix was found to vary by approximately 3-4 at% between the high and low Ni regions, with the O and C concentrations measured with EDS staying relatively unchanged. The inclusion region was found to have a lower Ni concentration compared to the high Ni matrix region, but was consistently identified to have a higher Ni content than the low Ni matrix regions using all methods. There was also a notable drop in O concentration and increase in the C concentration within the inclusion compared to the matrix which is attributed to the large cohenite and iron carbide grains present.

4. Discussion

4.1. Weathering of Nantan Fragment and Its Microstructure

Correlative microstructural analysis of the Nantan meteorite fragment using EDS, XRF, and XPS confirmed the elemental composition to be a majority Fe, Ni, and O, with no metallic Fe/Ni alloy found. The distribution of Ni was found using EDS, XRF, and XPS to be heterogeneous with large areas of higher Ni concentration (≥ 2.6 at%Ni), as shown in Fig. 2. Other elements common in weathering products, Si and C, were also found in this meteorite fragment.

It is believed this Nantan fragment underwent significant weathering since its fall due to the lack of non-oxide, e.g. kamacite or taenite, grains. XRD analysis of the polished sample surface showed a strong correlation magnetite and a weak correlation with goethite. This weaker correlation is likely due to limited amounts of goethite being exposed at the surface compared to magnetite. Simultaneous EDS-EBSD analysis confirmed the presence of these phases from the correlation of their experimental EBSPs to dynamical simulated patterns. EBSD analysis of the large inclusion also indicated the presence of cohenite, though this phase was not seen from XRD analysis. Overall, the major weathering products present in this Nantan fragment are believed to be magnetite, goethite, and cohenite.

The matrix of the sample was primarily made up of magnetite with areas of high Ni content. It is suggested that this Ni content is a result of kamacite that existed before weathering. Quantitative analysis of the high Ni region (green circle, Fig. 8) showed Fe:Ni ratios of 10:1 (27.8:2.8), 11:1 (29.29:2.67), and 9:1 (87.73:10.08), for EDS, XPS, and XRF respectively, or an average of 10:1. This ratio matches well with previously reported values of 9-19:1 for the Fe:Ni ratio of weathered materials from kamacite Binzel et al. (2006); Lee and Bland (2004); Palmer and Lauretta (2011). These Ni rich areas likely underwent an aqueous weathering process following equations 1 and 2. This weathering process also accounts for the presence goethite present in the sample. However, the final Ni species in this sample may be $\text{Ni}(\text{OH})_2$ rather than NiO based on the XPS results.

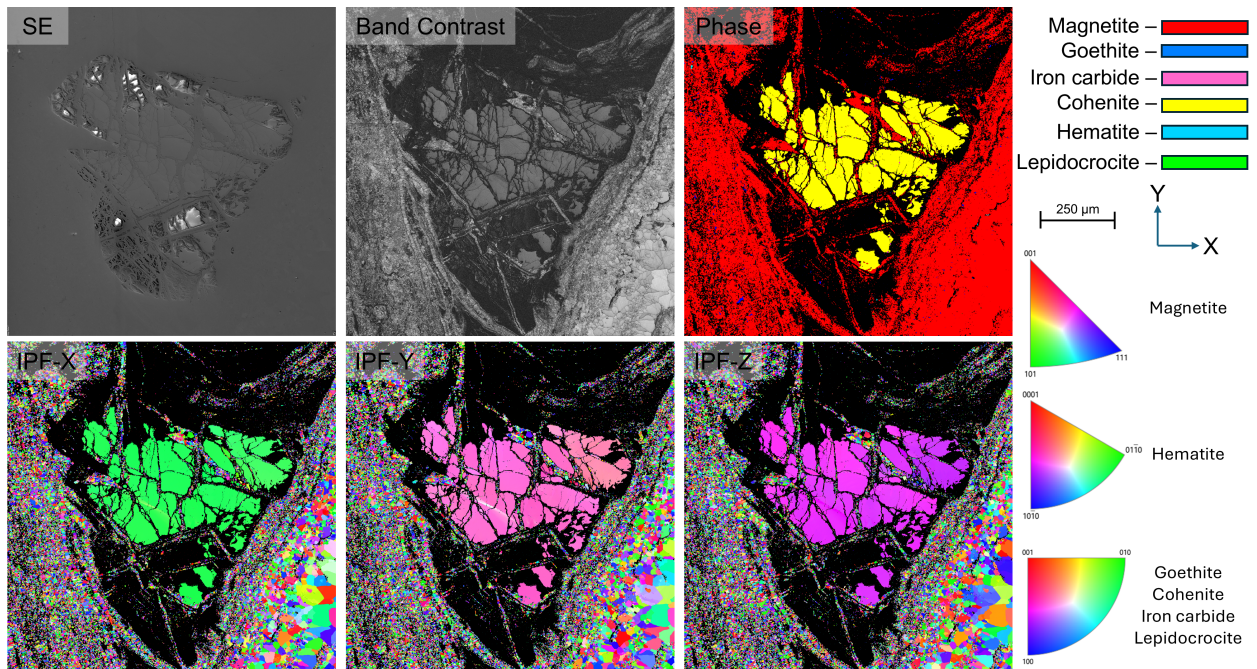


Figure 7: SE, Band Contrast, phase colour, and IPF maps of the large inclusion within the Nantan fragment captured using EBSD. The phase colour map shows the large fracture phase in the centre to be cohenite. The IPF maps show a rapid transition of grain size and that all the cohenite grains are in the same orientation.

The low Ni areas of the matrix are believed to have undergone a separate mechanism. Given the typical unweathered composition of iron meteorites being Fe,Ni-containing kamacite and taenite, it is likely that the remainder of the matrix formed through the dissolution of the Fe-Ni metal and subsequent oxidation and precipitation of the Fe. The lack of Ni in these regions after dissolution is likely due to Ni ions remaining in solution and being washed away. Unlike Fe, Ni does not oxidize past its bivalent state in weathering conditions and only precipitates as $\text{Ni}(\text{OH})_2$ above pH 7 White, Henderson and Mason (1967). This may also explain the $\text{Ni}(\text{OH})_2$ peaks seen in the high Ni region using XPS. It is suggested that the Ni content from these regions stayed in solution and was either removed from the meteorite or precipitated as $\text{Ni}(\text{OH})_2$ in different sections of the meteorite. However, it is unlikely that all of the original Ni stayed in solution to form $\text{Ni}(\text{OH})_2$ as NiO was seen to be present within the large inclusion.

The elemental composition and microstructure of the inclusion were found to be unique compared to the rest of the sample. In Fig. 6, and from the correlative analysis, there are four distinct regions and phases;

- Brecciated white inclusions - Fe, C, Ni ($(\text{Fe},\text{Ni})_3\text{C}$)
- Vein-like structure - Fe, Ni, O (Fe_3O_4 , NiO)
- Light grey cracked inclusions in voids - Ca, C, O (CaCO_3)
- Dark grey inclusions - Fe, C, O (FeCO_3)

It is likely that each of the carbide inclusion grains present in this region originated from a singular parent grain, as the IPF maps in Fig. 7 show each grain shares a common crystal orientation. The elemental composition and EBSD indexing indicate that this carbide phase is likely cohenite. The vein-like phase then formed as an extension of the high Ni section of the matrix through aqueous weathering and infiltration of the solution into the cracked cohenite, which is a common occurrence seen during oxidation of meteorites Binzel et al. (2006); Gooding (1986). The Fe and Ca-carbonates are secondary minerals which likely formed as part of the aqueous weathering process and incorporation of CO_3^{2-} from the local chemical environment Rubin (1997). The same weathering process which created the vein-like extension of the matrix also surrounded the inclusion in the high Ni matrix.

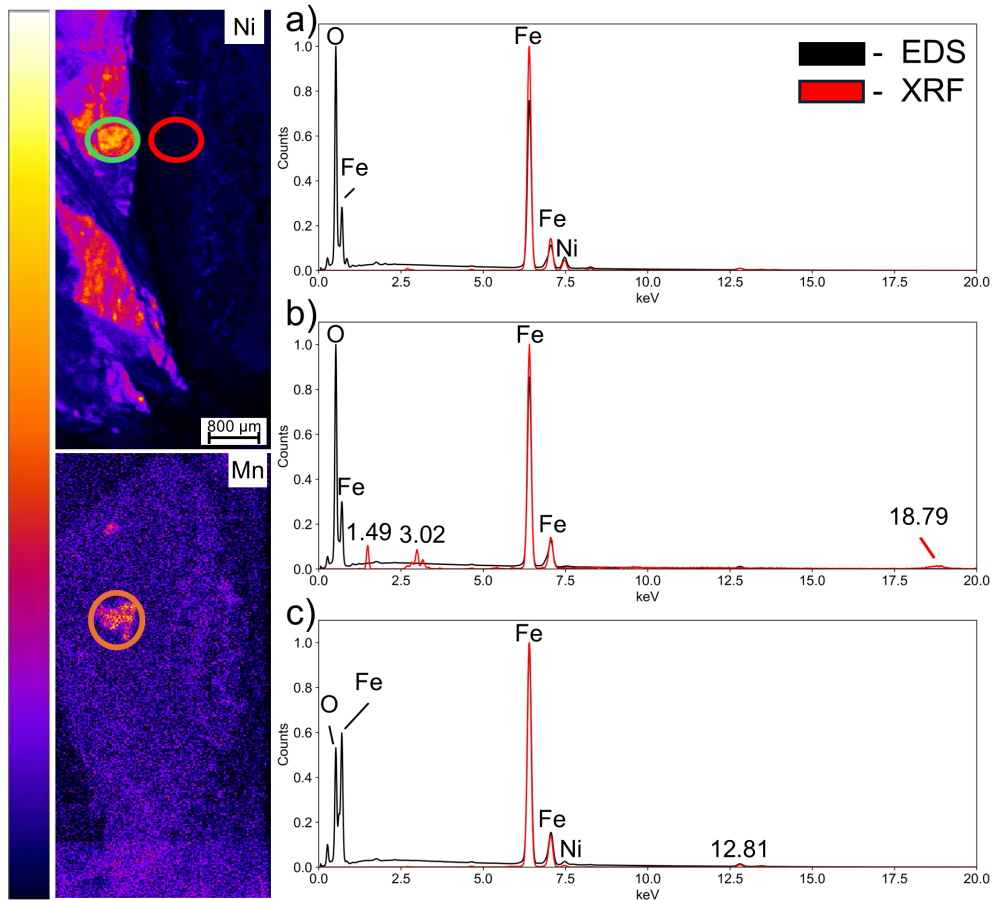


Figure 8: Overlaid EDS (black) and XRF (red) spectra for the three regions of interest, high Ni (green), low Ni (red), and the large inclusion (orange). The regions of analysis are circled on the XRF maps with their corresponding colours. The elemental composition for each regions determined using EDS are given on the right.

The unique grain structure seen in Fig. 7 can be attributed to the simultaneous grain formation during weathering and the grain refinement of Fe with the increase of Ni content. Weathering of the original kamacite matrix would have occurred over large areas of the material surface, causing a large number of grains to form simultaneously. This in combination with the known effect of Ni to reduce the grain size of iron alloys Pratomo, Oktadinata and Widodo (2019); Tong, Yao, Deng, Cheng, Chuang, Wang, Rao, Zhou and Wang (2021) results in the microstructure observed. It is not known if the increased presence of Ni itself or the weathering mechanism is the dominant contribution to this reduced grain size. However, a clear difference was seen in the grain structure of the high and low Ni sections of the matrix.

As seen in the lower right of the IPF maps in Fig. 7, the grain size of the matrix was seen to increase in size when transitioning from the high Ni to low Ni. Though the grain size was not observed to change immediately upon crossing the Ni boundary. Rather, a boundary region with width of 100-200 μm was seen surrounding the large inclusion and the high Ni section of the matrix where the Ni content decreased to ≤ 0.9 at% but the grain size did not increase.

Lastly, it is suggested that the inclusion region is a cross-section of a much larger feature within the meteorite fragment. The vein-like structure was seen to extend above the inclusion region using EDS (Fig. 2 a), with the Ni distribution having a similar fractured appearance to the inclusion. The Ni distribution also appeared to form a silhouette of a larger sub-surface feature which reaches a tip at the inclusion that was seen in the material surface.

4.2. Comparison of Techniques Used for Elemental Identification

EDS, XRF, and XPS all proved valuable in analyzing and evaluating the elemental composition across the sample and the weathering experienced by this Nantan meteorite fragment. All three techniques were capable of identifying the major metals, Fe and Ni, and visualizing how they were distributed. However, identification of additional elements was inconsistent across techniques.

An immediate limitation of XRF compared to XPS and EDS was the identification of C and O, as XRF has difficulties detecting elements with a Z number of 11 or lower without complex corrections. This was seen to be detrimental for quantitative elemental analysis of the Nantan fragment as the concentration of Fe and Ni were calculated to be skewed by $\geq 59\%$ higher than the other techniques. XRF was also found to perform well qualitatively for element mapping. It provided element maps of better resolution and visual quality than the XPS SnapMaps and a worse resolution but similar visual quality to EDS in a fraction of time (approx. 22 min vs. overnight), with the caveat that the step size was $20\ \mu\text{m}$ vs. $0.293\ \mu\text{m}$ for XRF and EDS respectively.

The penetration depth, step size and spot size were found to be important factors for each technique. Where the penetration depth is how far into a sample information can be gathered, step size is the spacing between individual measurements, and spot size is the area illuminated and sampled per measurement. The spot size of XPS was notably larger than in XRF, $200\ \mu\text{m}$ and $20\ \mu\text{m}$ respectively. Due to its larger spot size, the XPS provided maps of lower spatial resolution and was unable to identify the elemental composition of smaller phases in the sample. Phases with elements of lower concentration and sizes smaller than $200\ \mu\text{m}$ had their signal overwhelmed by that of the matrix, such as the Ca and Si bearing phases. This is a problem for geological samples and more specifically meteorites which commonly have phases of $\leq 50\ \mu\text{m}$ Lee and Bland (2004); Pirim et al. (2014); Francolini and Britton (2025). It is noted that XPS can have a smaller spot size in the 10s of micron range, but this size may still be problematic for small phases and inclusions. Additionally, XPS has the lowest penetration depth of the three techniques ($\leq 10\ \text{nm}$), compared to EDS ($\leq 10\ \mu\text{m}$) and XRF ($\geq 100\ \mu\text{m}$). This property is important when working with samples with oxide and carbon deposition layers, as these features make surface preparation and cleaning necessary for data acquisition. Such as the Ar^+ sputtering performed for XPS and fine mechanical polishing used in EBSD analysis. A summary of this information is given in Table 3.

Technique	Obtainable Information	Step/Spot Size (μm)	Penetration Depth	Accessible Elements
EDS	Composition, phase mapping	0.5-5	$\leq 10\ \mu\text{m}$	$Z \geq 2$
XPS	Composition, phase mapping, chemical state	200	$\geq 100\ \mu\text{m}$	$Z \geq 2$
XRF	Composition, phase mapping	20	$\leq 10\ \text{nm}$	$Z \geq 11$

Table 3

Comparison of elemental identification techniques. Spot/step sizes given are those used in this work.

While each technique has its limitations, each technique also has a unique benefit. XRF allows for rapid compositional analysis with minimal sample preparation and the ability to be performed outside a vacuum. This also allows for the use of XRF through hand-held devices Gemelli et al. (2015). XPS has the unique benefit in its ability to identify chemical states which is beneficial for mineral identification, especially when multivalent elements are present like Fe. Lastly, EDS can be used simultaneously with other techniques like EBSD and SEM without notably increasing acquisition time, allowing for a larger amount of information to be captured with low impact on the analysis time.

5. Conclusion

The Nantan fragment was found to have experienced extreme weathering, resulting in the sample to be composed of primarily magnetite with Ni hydroxide and Fe oxyhydroxides present. Two distinct regions of the matrix were seen using EDS, XPS, and XRF, a high ($\geq 2.6\ \text{at}\%$) and a low ($\leq 0.9\ \text{at}\%$) Ni concentration region. EDS determined the elemental composition in the high and low Ni regions of the matrix to be $(27.8 \pm 0.1)\ \text{Fe}-(2.8 \pm 0.1)\ \text{Ni}-(0.3 \pm 0.1)\ \text{Si}-(55.6 \pm 0.3)\ \text{O}-(13.4 \pm 0.1)\ \text{C}$ ($\text{at}\%$) and $(31.7 \pm 0.1)\ \text{Fe}-(0.2 \pm 0.1)\ \text{Ni}-(0.2 \pm 0.1)\ \text{Si}-(54.8 \pm 0.3)\ \text{O}-(13.1 \pm 0.1)\ \text{C}$ ($\text{at}\%$), respectively.

These high and low Ni concentration regions are believed to have found due to different weathering mechanisms occurring in the sample. The high Ni regions are believed to have been formed from the aqueous alternation of

kamacite into the chlorine stabilized akaganeite, which then decomposed into magnetite and goethite. This was further corroborated through identification and verification of goethite using XRD and EBSD. The low Ni regions are believed to have weathered through a direct dissolution and oxidation of Fe-Ni metal which resulted in the formation of magnetite and the washing away of Ni to form Ni(OH)₂. Other signs of weathering were also found in a large inclusion present at the analysis surface.

This inclusion was primarily composed of cohenite that appeared to be cracked, likely due to an impact the meteorite experienced. The cracks between the cohenite grains were found to be filled with a vein-like structure extending from the matrix and with small phases of Fe and Ca carbonate. The vein-like structure is believed to have formed during the aqueous alteration that formed the high Ni matrix, with the aqueous solution penetrating into the cracks of the cohenite.

The region of the matrix surrounding this large inclusion was also found using EBSD to have an unusual grain structure, with small grains (approx. 5 μm) that rapidly transitioned to grains 10s of μm in size. It is believed that this sudden transition in grain size and structure is related to the weathering process and the Ni content. However, a boundary of 100-200 μm in width was found to surround the high Ni content region of the matrix. The Ni content in this boundary region was found to match the low Ni content section of the matrix but the grains were found to retain their approx. 5 μm size.

Finally, it is suggested that this large inclusion is a small cross-section of a much larger feature within the meteorite body. The distribution of Ni was shown to form a silhouette that extended below the inclusion into a tip and above it with the same vein-like structure seen.

Acknowledgements

We acknowledge the following funding support: Natural Sciences and Engineering Research Council of Canada (NSERC) through their Discovery Grant program and the Vanier Canada Graduate Scholarship [Discovery grant: RGPIN-2022-04762, 'Advances in Data Driven Quantitative Materials Characterisation'], B.C. Knowledge Development Fund (BCKDF) and Canadian Foundation for Innovation through the Innovation Fund (CFI-IF) (#39798: AM+) and the John R. Evans Leaders Fund (CFI-JELF) [#43737, 3D-MARVIN]. We thank the Fipke Laboratory for Trace Element Research (FiLTER) at UBC Okanagan for provision of equipment for the XRF analysis. From Thermo Scientific, we acknowledge Helen Oppong-Mensah and Chris Stephens for the assistance with the MAPS software. Electron microscopy was performed at the Electron Microscopy Laboratory (Materials Engineering, UBC).

Appendix A. Supplementary Material

The supplementary material includes CIF files for each of the simulated XRD diffraction patterns given in Fig. 4. Those being, magnetite, goethite, hematite, cohenite, lepidocrocite, feroxyhyte, FeO(OH) high pressure, kamacite, taenite, and tetrataenite.

CRedit authorship contribution statement

Graeme J. Francolini: Conceptualization, Formal Analysis, Investigation, Methodology, Validation, Writing - original draft, writing - review and editing. **Brendan V. Dyck:** Investigation, Validation, Writing - review and editing. **Paul Mack:** Investigation. **Ben Britton:** Conceptualization, Supervision, Validation, Resources, Writing - review and editing.

Data Availability

Data will be released to Zenodo when the article is accepted for publication, and a DOI will be inserted here.

References

Allegretta, I., Marangoni, B., Manzari, P., Porfido, C., Terzano, R., De Pascale, O., Senesi, G.S., 2020. Macro-classification of meteorites by portable energy dispersive X-ray fluorescence spectroscopy (pED-XRF), principal component analysis (PCA) and machine learning algorithms. *Talanta* 212, 120785. URL: <https://www.sciencedirect.com/science/article/pii/S003991402030076X>, doi:10.1016/j.talanta.2020.120785.

- Bachmann, F., Hielscher, R., Schaebe, H., 2010. Texture Analysis with MTEX – Free and Open Source Software Toolbox. *Solid State Phenomena* 160, 63–68. doi:10.4028/www.scientific.net/SSP.160.63.
- Bender Koch, C., Buchwald, V.F., 1994. Weathering of Iron Meteorites from Monturaqui, Chile. *Meteoritics* 29, 443.
- Binzel, R.P., Walker, R.M., Cameron, A.G.W., 2006. Weathering of Chondritic Meteorites, in: Lauretta, D.S., McSween, H.Y. (Eds.), *Meteorites and the Early Solar System II*. University of Arizona Press, pp. 853–868. doi:10.2307/j.ctv1v7zdmm.
- Bland, P.A., Sexton, A.S., Jull, A.J.T., Bevan, A.W.R., Berry, F.J., Thornley, D.M., Astin, T.R., Britt, D.T., Pillinger, C.T., 1998. Climate and rock weathering: a study of terrestrial age dated ordinary chondritic meteorites from hot desert regions. *Geochimica et Cosmochimica Acta* 62, 3169–3184. doi:10.1016/S0016-7037(98)00199-9.
- Buchwald, V.F., Clarke, R.S., 1989. Corrosion of Fe-Ni Alloys by Cl-Containing Akaganeite β -FeOOH; the Antarctic Meteorite Case. *American Mineralogist* 74, 656–667.
- Chaves, L.C., Thompson, M.S., Loeffler, M.J., Dukes, C.A., Szabo, P.S., Horgan, B.H.N., 2023. Evaluating the effects of space weathering on magnetite on airless planetary bodies. *Icarus* 402, 115634. URL: <https://www.sciencedirect.com/science/article/pii/S0019103523002117>, doi:10.1016/j.icarus.2023.115634.
- Faust, G.T., Fahey, J.J., Mason, B.H., Dwornik, E.J., 1973. The disintegration of the Wolf Creek meteorite and the formation of pecoraite, the nickel analog of clinohyrosite. Technical Report 384-C. U.S. Govt. Print. Off. doi:10.3133/pp384C. ISSN: 2330-7102.
- Francolini, G.J., Britton, T.B., 2025. Microstructural characterization to reveal evidence of shock deformation in a Campo del Cielo meteorite fragment. *Materials Characterization* 222, 114838. doi:10.1016/j.matchar.2025.114838.
- Gemelli, M., D’Orazio, M., Folco, L., 2015. Chemical Analysis of Iron Meteorites Using a Hand-Held X-Ray Fluorescence Spectrometer. *Geostandards and Geoanalytical Research* 39, 55–69. doi:10.1111/j.1751-908X.2014.00291.x.
- van Ginneken, M., Debaille, V., Decrée, S., Goderis, S., Woodland, A.B., Wozniakiewicz, P., De Ceukelaire, M., Leduc, T., Claeys, P., 2022. Artificial weathering of an ordinary chondrite: Recommendations for the curation of Antarctic meteorites. *Meteoritics & Planetary Science* 57, 1247–1266. doi:10.1111/maps.13818. publisher: John Wiley & Sons, Ltd.
- Gooding, J.L., 1986. Weathering of stony meteorites in Antarctica. NTRS Author Affiliations: NASA Lyndon B. Johnson Space Center NTRS Document ID: 19860019346 NTRS Research Center: Legacy CDMS (CDMS).
- Goryunov, M.V., Varga, G., Dankházi, Z., Felner, I., Chukin, A.V., Kuzmann, E., Homonnay, Z., Grokhovskiy, V.I., Oshtrakh, M.I., 2023. Characterization of iron meteorites by scanning electron microscopy, X-ray diffraction, magnetization measurements, and Mössbauer spectroscopy: Gibeon IVA. *Meteoritics & Planetary Science* 58, 875–884. URL: <https://onlinelibrary.wiley.com/doi/abs/10.1111/maps.13984>, doi:10.1111/maps.13984.
- Gurdziel, A., 2015. Wietrzenie w meteorycie Nantan (porównanie wybranych wtórnych faz mineralnych z meteorytów Nantan i Morasko). *Acta Societatis Meteoriticae Polonorum*, 42–52.
- Karwowski, Ł., Gurdziel, A., 2009. SECONDARY MINERALS IN MORASKO AND PUŁTUSK METEORITES. *Visnyk of the Lviv University*, 243–248.
- Lee, M.R., Bland, P.A., 2004. Mechanisms of weathering of meteorites recovered from hot and cold deserts and the formation of phyllosilicates I. *Geochimica et Cosmochimica Acta* 68, 893–916. doi:10.1016/S0016-7037(03)00486-1.
- Leedahl, B., Korolev, A.V., Zhidkov, I.S., Skorniyakov, S.L., Anisimov, V.I., Belozherov, A.S., Kukharensko, A.I., Kurmaev, E.Z., Grokhovskii, V.I., Cholakh, S.O., Moewes, A., 2016. Searching for pure iron in nature: the Chelyabinsk meteorite. *RSC Advances* 6, 85844–85851. URL: <https://pubs.rsc.org/en/content/articlelanding/2016/ra/c6ra16598b>, doi:10.1039/C6RA16598B.
- Machado, A.S., de Araújo, O.M.O., Leitão, R.G., dos Anjos, M.J., de Oliveira, D.F., Lopes, R.T., 2025. Structural and Elemental Characterization of Martian Meteorites Using X-Ray Microtomography, X-Ray Microfluorescence, and Energy-Dispersive Spectroscopy. *X-Ray Spectrometry* 54, 632–642. URL: <https://onlinelibrary.wiley.com/doi/abs/10.1002/xrs.3500>, doi:10.1002/xrs.3500.
- Momma, K., Izumi, F., 2011. VESTA 3 for three-dimensional visualization of crystal, volumetric and morphology data. *Journal of Applied Crystallography* 44, 1272–1276. doi:10.1107/S0021889811038970. publisher: International Union of Crystallography.
- Palmer, E.E., Lauretta, D.S., 2011. Aqueous alteration of kamacite in CM chondrites. *Meteoritics & Planetary Science* 46, 1587–1607.
- Pirim, C., Pasek, M.A., Sokolov, D.A., Sidorov, A.N., Gann, R.D., Orlando, T.M., 2014. Investigation of schreibersite and intrinsic oxidation products from Sikhote-Alin, Seymchan, and Odessa meteorites and Fe3P and Fe2NiP synthetic surrogates. *Geochimica et Cosmochimica Acta* 140, 259–274. doi:10.1016/j.gca.2014.05.027.
- Pratomo, S.B., Oktadinata, H., Widodo, T.W., 2019. Effect of nickel additions on microstructure evolution and mechanical properties of low-alloy Cr-Mo cast steel. *IOP Conference Series: Materials Science and Engineering* 541, 012050. doi:10.1088/1757-899X/541/1/012050. publisher: IOP Publishing.
- Rubin, A.E., 1997. Mineralogy of meteorite groups. *Meteoritics & Planetary Science* 32, 231–247. doi:10.1111/j.1945-5100.1997.tb01262.x.
- Tong, Z., Yao, Q., Deng, J., Cheng, L., Chuang, T., Wang, J., Rao, G., Zhou, H., Wang, Z., 2021. Effects of Ni-doping on microstructure, magnetic and microwave absorption properties of CoFe2O4. *Materials Science and Engineering: B* 268, 115092. doi:10.1016/j.mseb.2021.115092.
- White, Jr., J.S., Henderson, E.P., Mason, B., 1967. Secondary Minerals Produced by Weathering of the Wolf Creek Meteorite. *American Mineralogist* 52, 1190–1179.
- Winkelmann, A., Jablon, B., Tong, V., Trager-Cowan, C., Mingard, K., 2020. Improving EBSD precision by orientation refinement with full pattern matching. *Journal of Microscopy* 277, 79–92. doi:10.1111/jmi.12870.